

Cite this: *J. Mater. Chem. C*, 2023,  
11, 2911

## Quantifying electrochemical losses in perovskite solar cells†

Tulus,<sup>a</sup> Junke Wang,<sup>b</sup> Yulia Galagan<sup>c,d</sup> and Elizabeth von Hauff<sup>e,f</sup>

We quantify electrochemical losses in perovskite solar cells (PSCs) based on methylammonium lead triiodide (MAPbI<sub>3</sub>) films with impedance analysis. We focus on the characteristic signatures of impedance spectra taken from PSCs, in particular the negative capacitance hook widely observed in the low frequency regime. We elucidate the underlying physical origin for the negative capacitance by applying a generalized equivalent circuit model (ECM) for PSCs that accounts for fast electrical dynamics resulting in high frequency (HF) signatures due to electronic processes, and much slower electrochemical dynamics that result in low frequency (LF) signatures in the spectra. We observe relaxation times faster than 10<sup>-6</sup> s in the HF regime that can be attributed to electrical dynamics, while relaxation times longer than 10<sup>-3</sup> s in the LF regime that are consistent with electrochemical dynamics. The voltage-dependence and timescales of the electrochemical dynamics are consistent with MA<sup>+</sup> and I<sup>-</sup> migration in the MAPbI<sub>3</sub> absorber layer. At higher applied voltages, we observe a highly non-linear response from the PSC which is consistent with irreversible chemical changes in the MAPbI<sub>3</sub> absorber. We demonstrate how ECM modelling combined with the analysis of ECM fit quality is a useful approach for *in situ* monitoring and quantitative diagnosis of loss mechanisms in PSC.

Received 18th August 2022,  
Accepted 31st January 2023

DOI: 10.1039/d2tc03486g

rsc.li/materials-c

## 1. Introduction

Metal halide perovskite solar cells (PSCs) are an emerging technology that has demonstrated unprecedented increases in power conversion efficiencies (PCE) over the last decade.<sup>1-6</sup> Advances in PSC device performance have been achieved *via* the optimization of fabrication protocols, new compositions, and stabilization of the perovskite absorber layer.<sup>7,8</sup> PSCs have good potential to become an efficient and low-cost thin-film photovoltaic (PV) technology.<sup>7-10</sup> The current record efficiency of PSC are over 25%.<sup>11-15</sup> Reduction in charge carrier recombination, which fundamentally limits the fill factor (FF) and the open-circuit voltage ( $V_{oc}$ ), is necessary to increase PSCs efficiency towards the thermodynamic limit.<sup>7-9,16-19</sup> However, the performance of even state-of-the-art PSC are ultimately limited by losses at the device

interfaces,<sup>7,11,16,20-22</sup> and therefore more efforts are required to understand interfacial losses during device operation.

Methylammonium (MA) lead triiodide (CH<sub>3</sub>NH<sub>3</sub>PbI<sub>3</sub>) – or MAPbI<sub>3</sub> – is a perovskite absorber layer that was widely used in the first generation of PSC.<sup>1,23-25</sup> From all the single-halide absorber layers *i.e.* MAPbI<sub>3</sub>, MAPbBr<sub>3</sub>, MAPbCl<sub>3</sub>, FAPbI<sub>3</sub> (FA: Formamidinium), FAPbBr<sub>3</sub> and FAPbCl<sub>3</sub>; MAPbI<sub>3</sub> has the most appropriate bandgap for photovoltaic energy conversion, as Br and Cl-based absorber layers have larger bandgaps and therefore comparatively reduced light harvesting potential.<sup>26-28</sup> In this context, MAPbI<sub>3</sub> and FAPbI<sub>3</sub> may be the most promising PSC absorbers for PV applications.<sup>8,29</sup> However, FAPbI<sub>3</sub> has been reported to have poor structural stability at room temperature, and can crystallize either into a photo-inactive, non-perovskite hexagonal  $\delta$ -phase (yellow phase) or a photoactive perovskite  $\alpha$ -phase (black phase), which is sensitive to solvents or humidity.<sup>30</sup> In the case of MAPbI<sub>3</sub>, instability of the absorber layer has been linked to the thermally unstable and reactive MA<sup>+</sup> ion<sup>31,32</sup> as well as to the mobile I<sup>-</sup> ion.<sup>5,26-28</sup> While the larger ionic radius of Br<sup>-</sup> in MAPbBr<sub>3</sub> absorbers results in better stability, this stability comes at the cost of a less optimal bandgap for PV energy conversion.<sup>26,27</sup>

In early studies, MAPbI<sub>3</sub> films were produced from a solution of methylammonium iodide (MAI) and lead(II) iodide (PbI<sub>2</sub>) using a two-step deposition process that yielded low quality films with pinholes.<sup>9,33,34</sup> Advances in the processing and understanding of MAPbI<sub>3</sub> film formation has resulted in more stable films.<sup>18,33</sup> Recent studies demonstrated that one-step deposition that does not incorporate anti-solvent, but does include trace amounts of

<sup>a</sup> Physics of Energy, Department of Physics & Astronomy, Faculty of Sciences, Vrije Universiteit Amsterdam, 1081 HV, Amsterdam, The Netherlands.

E-mail: elizabeth.von\_hauff@tu-dresden.de

<sup>b</sup> Research Center for Advanced Materials, National Research & Innovation Agency (BRIN), Jakarta, 10340, Indonesia

<sup>c</sup> TNO – Solliance, 5656 AE, Eindhoven, The Netherlands

<sup>d</sup> National Taiwan University, Department of Materials Science and Engineering, Taipei, 106, Taiwan

<sup>e</sup> Faculty of Electrical and Computer Engineering, Technical University of Dresden, Dresden, Germany

<sup>f</sup> Fraunhofer Institute for Organic Electronics, Electron Beam and Plasma Technology (FEP), Dresden, Germany

† Electronic supplementary information (ESI) available. See DOI: <https://doi.org/10.1039/d2tc03486g>



water, yields larger perovskite crystals with less defects,<sup>35</sup> resulting in higher quality films.<sup>34–37</sup> While mixed cation, mixed halide PSC have yielded the best efficiency and stability results to date,<sup>11,38–41</sup> processing single cation, single halide PSC is more straightforward for industrially-relevant fabrication protocols and up-scaling.<sup>6,7,9,10,42,43</sup> In this study, we focus on the well-known PSC system MAPbI<sub>3</sub>, fabricated with an optimized one-step process.<sup>9,34,36,44</sup>

The instability of PSC has been linked to the mixed conduction of ionic and electrical carriers in the perovskite absorber, including ion accumulation at the device interfaces.<sup>45–49</sup> These electrochemical dynamics can be detrimental to PSC stability, as they result in charge rearrangement and therefore a change in the electrostatic environment in the absorber layer.<sup>45–49</sup> This, in turn, impacts the electrical dynamics, *i.e.* charge transport and recombination, in the solar cell.<sup>45</sup>

In this study, we applied impedance spectroscopy (IS) to identify and quantify electrochemical losses in PSC based on MAPbI<sub>3</sub>, as the physical interpretation of the low frequency features in the IS spectra of these devices remains unclear.<sup>50–52</sup> We investigate MAPbI<sub>3</sub> fabricated using an optimized one-step process in a standard device architecture,<sup>34,36,44,45,53–55</sup> as a model system. We used photoluminescence spectroscopy (PL) and X-ray diffraction analysis (XRD) to confirm the structure and quality of the MAPbI<sub>3</sub> film. We then applied IS combined with a generalized equivalent circuit model (ECM) analysis<sup>45,56</sup> that allows us to distinguish between electrical and electrochemical dynamics in the PSC. From the ECM we are able to estimate the dielectric constant of the MAPbI<sub>3</sub> layer, and quantify the timescales of the electrochemical dynamics. We apply a Kramers–Kronig analysis to analyze the quality of the ECM fit in order to elucidate the nature of the loss processes in the PSC.

## 2. Result

### 2.1. MAPbI<sub>3</sub> film structure

We fabricated MAPbI<sub>3</sub> films according to the optimized one-step protocol in the Experimental section. To verify the quality of the films, we performed XRD to confirm the crystallinity, and optical studies with PL spectroscopy to confirm the low defect density in the films. Fig. 1(a) shows XRD pattern of the MAPbI<sub>3</sub> perovskite

film on glass. We observe prominent peaks that are consistent with the MAPbI<sub>3</sub> crystal structure at  $2\theta = 14^\circ$  (110),  $28^\circ$  (220) and  $43^\circ$  (330), respectively.<sup>34–36,44</sup> Fig. 1(b) shows the PL (red line); and absorption properties (blue line), of MAPbI<sub>3</sub> film on glass after thermal annealing, respectively. We observed a sharp peak in the PL spectrum at 1.60 eV (773 nm) corresponding to bandgap energy of MAPbI<sub>3</sub>, which is consistent with previous reports<sup>34,35,44</sup> as well as with the absorption spectrum. We note that the bandgap of our MAPbI<sub>3</sub> perovskite films are narrower (1.60 eV) than that of MAPbI<sub>3</sub> fabricated *via* a two-step deposition (1.50 eV).<sup>57,58</sup>

### 2.2. Solar cells characteristics

PSCs were fabricated with the planar structure: ITO/TiO<sub>2</sub>/MAPbI<sub>3</sub>/Spiro-OMeTAD/Au. The TiO<sub>2</sub> serves as an electron transport layer (ETL) and the spin-cast Spiro-OMeTAD layer serves as the hole transport layer (HTL) in the device. A total of 28 devices were fabricated and measured for this study. Fig. 2(a) is a schematic of the solar cell architecture investigated in this study, and Fig. 2(b) shows the current density–voltage (*J*–*V*) characteristics of the champion PSC in the dark (black) and under standard AM 1.5 illumination before (blue) and after (red) light soaking. We depict the reverse scan here. The PSC was subjected to light soaking (2 minutes) immediately before the *J*–*V* measurement. We note a slight change in the solar cell parameters after light soaking. The PCE of the champion cells increased from 16.71% to 17.45%, the *V*<sub>oc</sub> increased from 980.42 mV to 1025.27 mV, and the FF increased from 77.89% to 78.10% after light soaking. The short-circuit current density (*J*<sub>sc</sub>) however decreases slightly after light soaking from 21.88 mA cm<sup>−2</sup> of 21.79 mA cm<sup>−2</sup>.

Fig. 3 shows the solar cells parameters from the 28 solar cells measured, and the data were fit with a Gaussian to extract the mean values as well as the standard deviation in the solar cell parameters: (a) PCE = 13.60% ± 3.61%, (b) *J*<sub>sc</sub> = 20.09 mA cm<sup>−2</sup> ± 3.47 mA cm<sup>−2</sup>, (c) *V*<sub>oc</sub> = 1033.16 mV ± 35.25 mV, and (d) FF = 66.92% ± 18.62%. Table 1 summarizes the solar cell parameters from the champion cell before and after light soaking, as well as the mean values from the 28 devices.

The change in *V*<sub>oc</sub>, FF, and *J*<sub>sc</sub> upon light soaking are consistent with reports of light induced trap filling<sup>21,59,60</sup> or curing<sup>59,61,62</sup> at the perovskite/TiO<sub>2</sub> interface.

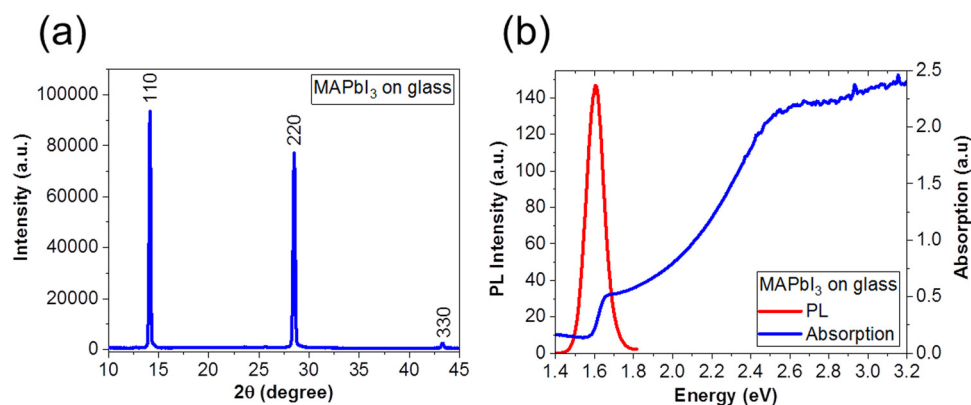


Fig. 1 (a) XRD pattern and (b) PL (red line) and absorption (blue line) spectra of a MAPbI<sub>3</sub> film on glass substrate.



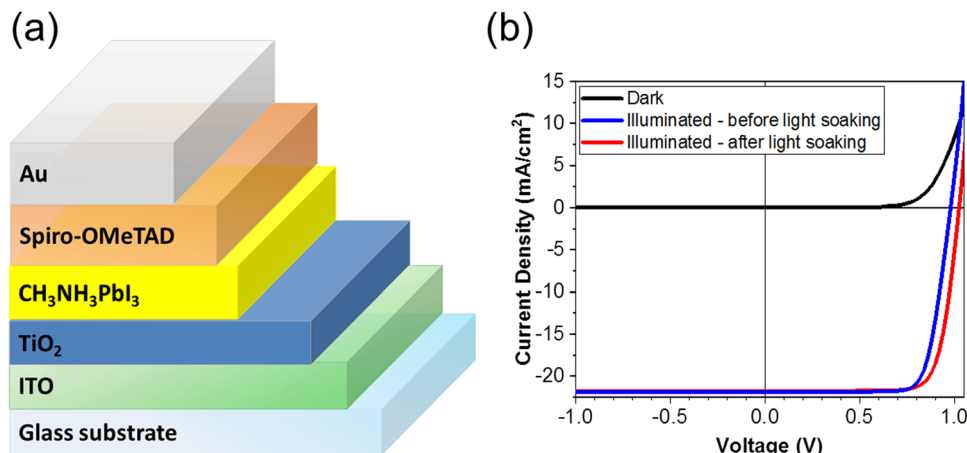


Fig. 2 (a) Schematic of the PSC architecture, (b) the  $J$ - $V$  characteristics of the PSC under dark (black), and under standard AM 1.5 illumination before (blue) and after (red) light soaking.

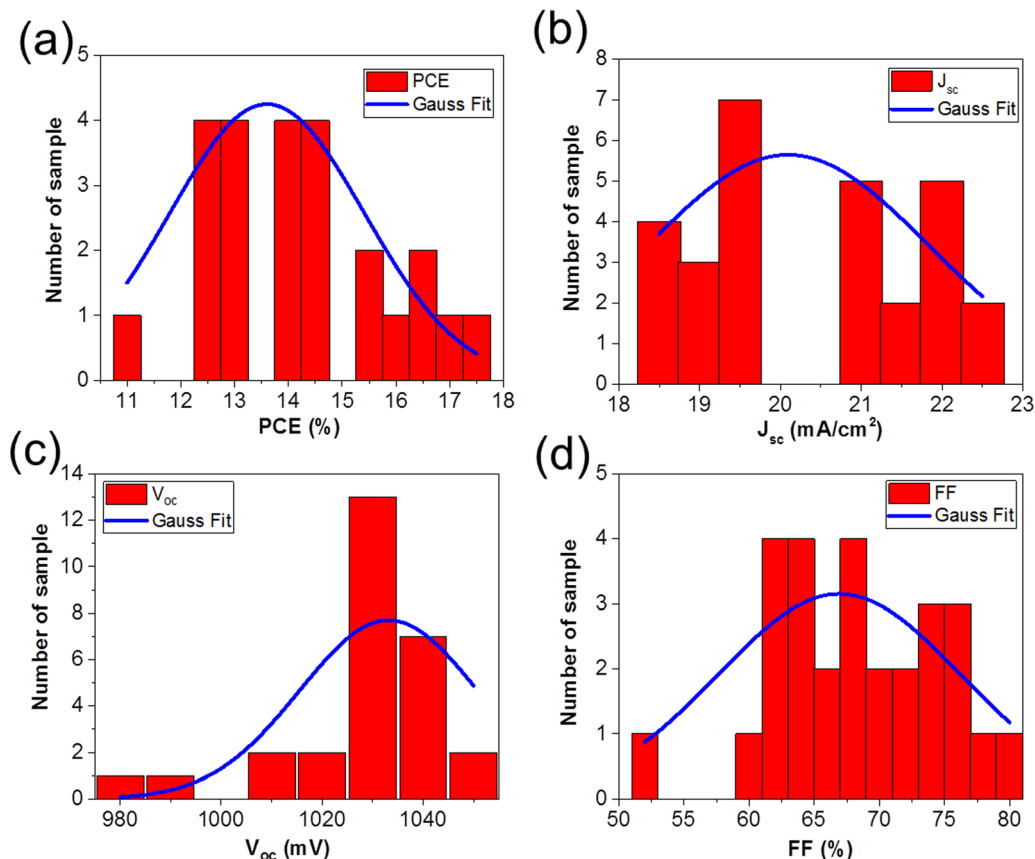


Fig. 3 Variation in the solar cell parameters from the 28 devices studied (red bars). The data were fit with a Gaussian distribution (blue line) to determine the mean values and standard deviation for the (a) PCE =  $13.60\% \pm 3.61\%$ , (b)  $J_{sc} = 20.09 \text{ mA cm}^{-2} \pm 3.47 \text{ mA cm}^{-2}$ , (c)  $V_{oc} = 1033.16 \text{ mV} \pm 35.25 \text{ mV}$ , and (d) FF =  $66.92\% \pm 18.62\%$ , respectively.

### 2.3. Quantifying electrochemical dynamics in MAPbI<sub>3</sub> PSC

During an IS measurement, the PSC is subject to an external bias and often illumination over many minutes. It is therefore generally challenging to obtain reliable IS data sets<sup>45,63,64</sup> from PSC under these conditions, except at  $V_{oc}$ . Therefore, we specifically chose to investigate the IS from the PSC in the dark as a function of the

external applied voltage. This allowed us to study and quantify the voltage-dependence of electrochemical dynamics in the PSC under controlled conditions, and to isolate these effects from more complex photo-activated (and irreversible) dynamics in the device.

We investigated the IS at applied DC voltage offsets of 0.7 V, 0.8 V, 0.9 V, and 1.0 V. Fig. 4 shows the Nyquist plots of the



**Table 1** The solar cell parameters for the champion cell before and after light soaking, and the mean values and standard deviation of the solar cell parameters from 28 PSCs

Sample	Condition	$V_{oc}$ (mV)	$J_{sc}$ ( $\text{mA cm}^{-2}$ )	FF (%)	PCE (%)
Champion cell	Before light soaking	980.42	21.88	77.89	16.71
	After light soaking	1025.27	21.79	78.1	17.45
Average from 28 devices	After light soaking	$1033.16 \pm 35.25$	$20.09 \pm 3.47$	$66.92 \pm 18.62$	$13.60 \pm 3.61$

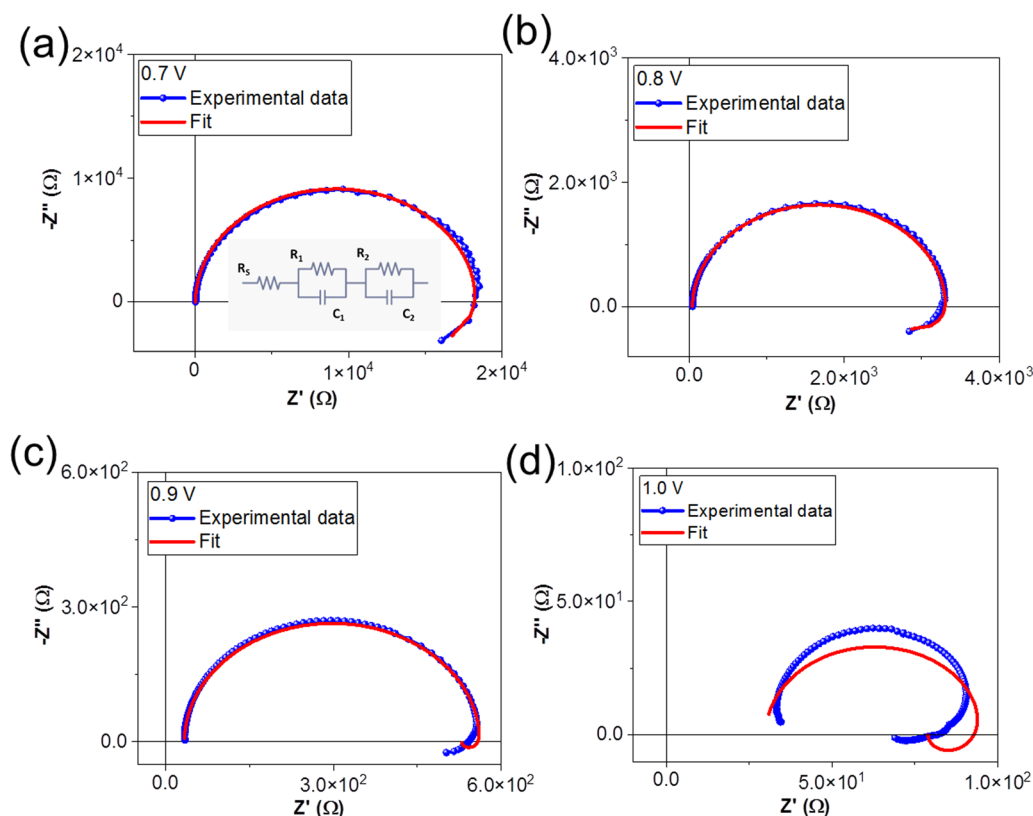


**Fig. 4** Nyquist plots of experimental data and ECM fits at (a) 0.7 V, (b) 0.8 V, (c) 0.9 V and (d) 1.0 V. The ECM used to fit the data is shown in the inset of (a).

experimental data (blue) and fits at voltages of (a) 0.7 V, (b) 0.8 V, (c) 0.9 V and (d) 1.0 V. The Nyquist plots display the characteristic form for PSC: a high frequency (HF) semicircle and a low frequency (LF) feature, including hooks and/or tails.<sup>45,50,51,65</sup> Specifically, our data reveal a LF negative capacitance (see ESI† in Fig. S1(c)). The HF dynamics are attributed to fast electrical dynamics, such as transport and recombination, in the PSC. The reported timescales of these electrical dynamics are highly comparable in PSC devices, independently of the composition of the absorber layer or ETL and HTL materials. In contrast, the slower LF dynamics, attributed to electrochemical dynamics, and are strongly dependent on the quality and stability of the materials and interfaces in the PSC.<sup>45,56</sup> Strictly speaking, the HF and LF dynamics are interdependent in PSC, as the rearrangement of the ionic species in the PSC influences the electrostatic environment in the absorber layer and therefore changes the electrical transport dynamics in the device.<sup>46,66</sup> However, electrical dynamics are orders of magnitude faster

than electrochemical dynamics, and therefore the HF and LF signatures are separated by several orders of magnitude in the IS frequency spectrum. This means that the IS from the PSC can be modelled with a general ECM comprised of two independent, serially connected resistor–capacitor (RC) elements to account for the HF and LF dynamics.<sup>45</sup>

We fit the IS data using the generalized ECM shown in the inset of Fig. 4(a), where  $R_s$  accounts for the series resistance,  $R_1C_1$  accounts for the HF dynamics, and  $R_2C_2$  accounts for the LF electrochemical dynamics. The time constant ( $\tau$ ) of the RC element ( $\tau = R.C$ ) corresponds to the relaxation times of the dynamics. We note that the ECM fits the IS data measured at DC voltages of 0.7 V, 0.8 V and 0.9 V, but that the fits are very poor for spectra taken at 1.0 V. The values of the circuit elements from the ECM are summarized in Table 2.

We discuss the voltage-dependence of the series resistance,  $R_s$ , followed by the HF response  $R_1C_1$  and the respective timescale  $\tau_1$ , and finally the LF response,  $R_2C_2$  and the respective timescale  $\tau_2$ .



**Table 2** Parameters extracted from the ECM analysis of IS measured at DC bias of 0.7 V, 0.8 V, 0.9 V, and 1.0 V in the dark, respectively

DC offset (V)	$R_S$ ( $\Omega$ )	$R_1$ ( $\Omega$ )	$C_1$ (F)	$R_2$ ( $\Omega$ )	$C_2$ (F)
0.7	42.47	18 446.0	$178.42 \times 10^{-8}$	-7321.00	$-3.89 \times 10^{-6}$
0.8	37.14	3280.0	$183.98 \times 10^{-8}$	-751.70	$-1.76 \times 10^{-5}$
0.9	33.58	529.3	$189.68 \times 10^{-8}$	-33.19	$-3.32 \times 10^{-5}$
1.0	29.95	68.9	$198.68 \times 10^{-8}$	-19.92	$-9.29 \times 10^{-7}$

We attribute the decrease in the series resistance  $R_S$  with applied voltage to changes in the electrical properties of the  $\text{TiO}_2$  due to current flow, *i.e.* trap filling.<sup>59,60</sup>

The HF circuit element  $R_1C_1$  models the cumulative electrical dynamics in the PSC, and it is not possible to elucidate individual dynamics associated with transport and recombination processes. This assumption relies, on one hand, results from recent studies that combined electrical characterization and modelling to show that time and frequency-resolved electrical characterization (such as IS) cannot directly access electrical dynamics in the PSC, but instead probe the change in the electrical transport resulting from slower electrochemical dynamics that change the electrostatic environment during the measurement.<sup>46,47,66</sup> Secondly, it is based on the fact that the geometric capacitance ( $C_{\text{geo}}$ ) of the PSC, as the lowest capacitance in series, dominates at high frequencies, thereby making it impossible to de-convolute individual dynamics.<sup>45</sup> It should be noted, however, that changes in  $R_1C_1$  in response to voltage, illumination, and more specifically, in response to environmental stress are useful for monitoring PSC performance.<sup>51</sup> Therefore,  $R_1$  is an effective resistance that contains all of the electrical contributions (transport, recombination) to resistance at high frequencies. We exploit the fact that  $C_{\text{geo}}$  dominates  $C_1$  to estimate the relative permittivity ( $\epsilon$ ) of the perovskite absorber layer according to

$$\epsilon = \frac{C_{\text{geo}}D}{\epsilon_0 A} \approx \frac{C_1 D}{\epsilon_0 A} \quad (1)$$

where  $\epsilon_0$  is the permittivity of free space,  $D$  is the thickness of perovskite layer in the devices, and  $A$  is the device area. We obtain a value of  $\epsilon = 69.30$  (at 0.8 V), which is consistent with previous reports for  $\text{MAPbI}_3$ .<sup>28,67</sup> We observe that  $R_1$  decreases with applied voltage, which is consistent with an increase in the current density in the PSC.  $C_1$  increases slightly with voltage, indicating that the chemical capacitance of injected carriers may also contribute minimally to the HF capacitance at higher applied voltages. Fig. 5 shows the corresponding HF relaxation times  $\tau_1$  and LF relaxation times  $\tau_2$  versus applied external voltage. The HF dynamics ( $\tau_1$ ) decrease exponentially with applied DC voltage. This is a result of the exponential decrease in  $R_1$  with voltage, consistent with the exponential increase in the current density according to the diode equation (see ESI† in Fig. S2 and S3(a)). The values of  $C_1$  are essentially voltage-independent (see ESI† in Fig. S3(b)), since  $C_1$  is dominated by  $C_{\text{geo}}$ , and the relative permittivity is not a voltage-dependent parameter.

The LF circuit element  $R_2C_2$  models the slower electrochemical dynamics in the PSC. We note that both  $R_2$  and  $C_2$

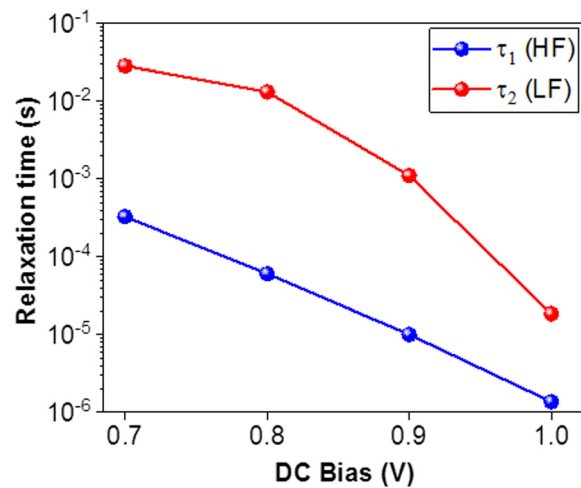


**Fig. 5** The relaxation times  $\tau_1$  (HF) and  $\tau_2$  (LF) versus applied DC bias.

are negative for all voltages, corresponding to the negative capacitive tail observed in the Nyquist plots. Negative resistances are correlated with processes that promote current flow, while negative capacitances occur when the AC current response leads the AC voltage excitation, *i.e.* capacitive discharge. This behavior is consistent with the neutralization of trap states in the PSC and/or improved band bending at the device interface,<sup>45</sup> and has been very frequently observed at high voltage in organometal tri-halide PSCs based on  $\text{MAPbI}_3$  and  $\text{MAPbBr}_3$ .<sup>65</sup> Analogously to  $R_1$ ,  $R_2$  decreases with voltage. However,  $R_2$  is more than an order of magnitude lower than  $R_1$  at each applied voltage and the values are negative. The  $C_2$  values are also negative, and are between one and three orders of magnitude larger than  $C_1$ . In contrast to the other circuit elements,  $C_2$  does not follow any clear trend with applied voltage (see ESI† in Fig. S3(a and b)). The LF time constant  $\tau_2$  is positive and larger than the HF time constant  $\tau_1$  (consistent with the slower dynamics), and decreases with applied voltage. At 1.0 V,  $\tau_1 = 1.37 \times 10^{-6}$  s and  $\tau_2 = 1.85 \times 10^{-5}$  s, and at this point, the timescales of the HF and LF dynamics become comparable. We observed that there is no longer obtain a linear response in the IS from the PSC at higher applied voltages.

The migration of  $\text{I}^-$  and  $\text{MA}^+$  ions in  $\text{MAPbI}_3$ ,<sup>68</sup> as well as the formation of  $\text{PbI}_2$ ,<sup>68,69</sup> and  $\text{PbI}_6$  in  $\text{MAPbI}_3$  films deposited on  $\text{TiO}_2$  substrates<sup>35,61,62,70</sup> has been widely reported. This results in transient behavior of the electrical properties of  $\text{MAPbI}_3$  PSC, which has been correlated with voltage-dependent variations in local ionic concentration.<sup>59,64,68</sup> Under open circuit conditions, the  $\text{MA}^+$  ions accumulate at the ETL, while the  $\text{I}^-$  ions accumulate at the HTL, while under applied forward bias,  $\text{MA}^+$  ions drift away from the HTL interface, while the negatively charged  $\text{I}^-$  ions drift away from the ETL, respectively. Futscher *et al.*<sup>68</sup> performed temperature-dependent transient ion drift measurements on  $\text{MAPbI}_3$  PSC and found that the concentration of  $\text{MA}^+$  ions is generally one order of magnitude higher than the concentration of  $\text{I}^-$  ions, and reported transients associated with  $\text{MA}^+$  on the order of seconds, depending on the fabrication of the PSC while  $\text{I}^-$  transients are faster (less than ms) and



comparable between different MAPbI<sub>3</sub> PSC. Additionally, the sensitivity of MAPbI<sub>3</sub> absorber layers to moisture has been widely reported.<sup>35,36,71</sup> While trace amounts of water<sup>35</sup> and water vapor<sup>71</sup> introduced either *via* the precursors or during post processing of the MAPbI<sub>3</sub> layer can impact crystal size and quality, liquid water can promote the chemical degradation of the absorber,<sup>36,71</sup> resulting in the formation of PbI<sub>2</sub>. Our XRD results do not indicate the formation of PbI<sub>2</sub> and our measurements were performed under an N<sub>2</sub> atmosphere. Therefore, we do not expect water-induced degradation in our samples, although we cannot fully exclude the impact of trace amounts of water introduced over the precursors on the LF signature.

In order to understand the LF dynamics in more detail, we apply a Kramers–Kronig (KK) check. Generally, KK checks are applied to confirm the quality of the IS spectra for analysis and modelling.<sup>64,72–74</sup> IS spectra must satisfy the basic criteria of linearity, stability, causality, and finiteness, however the slow electrochemical dynamics can impact both stability and causality during the measurement leading to deviations from the ideal linear response. We exploit deviations from the KK relations in our IS data in order to elucidate the underlying nature of the LF dynamics at different applied voltages. Specifically, we examine the frequency-dependence of the residuals from the KK test to identify the timescales at which the KK relations deviate from the expected linear behavior. The KK fit is performed by fitting the spectra with a linear series of RC elements, typically between 5–20. The number of RC elements in the circuit is increased until a good fit is achieved, and the residuals indicate the difference between the fit and the experimental data. The rationale behind this approach is that KK-compliant IS data can be fit with an infinite chain of RC elements. However, the ECM used for the KK fit does not necessarily have any relevance for the physical interpretation, as it is likely over-dimensioned.<sup>63</sup> As a rule of thumb, residuals < 0.5% are accepted in the literature to indicate good agreement between experiment and the KK fit.<sup>50,63,64</sup>

Fig. 6(a–d) shows the experimental data (blue) and the KK fit (red) of Re(Z) and Im(Z) *versus* frequency at a DC bias of 0.7 V, 0.8 V, 0.9 V, and 1.0 V, respectively. Fig. 6(e–h) show the residuals from the KK fit *versus* frequency; at DC bias of 0.7 V, 0.8 V, 0.9 V, and 1.0 V, respectively. The orange data represents the residual from Re(Z) and the pink data represents the residual from Im(Z), respectively. The frequencies that correspond to the relaxation times ( $\tau_1$  and  $\tau_2$  shown in Fig. 5) are marked with a vertically dashed line in each spectrum (HF (blue) and LF (red)), while the highlighted (gray) region corresponds to the frequency range where the negative capacitive tail is observed in the Nyquist plot.

We observe reasonable agreement between the experimental data and the KK fits for DC biases of 0.7 V, 0.8 V, and 0.9 V (<2%), except at 1.0 V (>2%), which is consistent with the poor fit of the ECM at 1.0 V. We classify the offsets in the KK residuals into four different frequency regimes. At low frequencies ( $10^1 \text{ Hz} \leq f \leq 10^2 \text{ Hz}$ , corresponding to timescales between  $10^{-3}$ – $10^{-2}$  s), we observe a constant offset in the residuals at all applied voltages that increases in magnitude with increasing voltage. At low-intermediate frequencies ( $10^2 \text{ Hz} \leq f < 10^4 \text{ Hz}$ ,

corresponding to timescales between  $10^{-5}$ – $10^{-3}$  s), we observe the emergence of a further voltage-dependent offset in the residuals at voltages of 0.8 V and higher. At high-intermediate frequencies ( $f \approx 10^5 \text{ Hz}$ , corresponding to timescales around  $10^{-6}$  s), we observe a weakly voltage-dependent offset that overlaps strongly with lower and higher frequency offsets at increasing voltage. Finally at high frequencies ( $f > 10^5 \text{ Hz}$ , corresponding to timescales lower than  $10^{-6}$  s), we observe a large offset that we attribute to the capacitive effects of the cables, which is consistent with the literature.<sup>63</sup>

The timescales associated with the low and low-intermediate frequency offset in the KK-residuals ( $f < 10^3 \text{ Hz}$ ) are consistent with timescales of ionic transport,<sup>45</sup> and more specifically these timescales are comparable to values reported for MA<sup>+</sup> (s) and I<sup>−</sup> (ms) ion migration in MAPbI<sub>3</sub> PSC,<sup>68</sup> respectively. This interpretation is consistent with results from a recent report from Reichert, *et al.*<sup>75</sup> who applied transient electrical studies to identify the activation energies of distinct interfacial defect states related to the voltage-dependent migration of MA<sup>+</sup> and I<sup>−</sup> ions, as well as a reports on the voltage-dependent kinetics associated with ion/vacancy surface interactions.<sup>65</sup>

The concentration of MA<sup>+</sup> ions is higher than I<sup>−</sup> ions and the transport of MA<sup>+</sup> slower than I<sup>−</sup> ions, therefore we expect the MA<sup>+</sup> ions dominate the LF signature in the IS data. The negative capacitive hook observed in the Nyquist plot as well as the  $\tau_2$  values are within this LF range, indicating that the LF dynamics are dominated by ionic, specifically MA<sup>+</sup> migration. However, we note that the LF dynamics are a convolution of all ionic dynamics, including the diffusion coefficients, concentrations, and activation energies. This is consistent with the lack of clear voltage-dependence we observe in  $C_2$ , as the voltage-dependence of LF combines the independent contributions of the MA<sup>+</sup> and I<sup>−</sup> ionic distributions. The high-intermediate frequency regime corresponds to timescales on the order of  $10^{-5}$  s, which has been attributed in the literature to electrode polarization and carrier detrapping.<sup>45,50</sup> Since we are examining KK-residuals, *i.e.* deviations from the linear response, we are more confident about attributing the dynamics in this frequency range to electrode polarization due to ion migration. While ionic transport may generally be reversible, the IS measurements are performed under a constant applied DC offset bias. Therefore, ion migration (which is much slower than electrical transport) behaves as an irreversible process and leads to the KK residuals in the corresponding frequency regime. Finally, we note that the poor ECM fit and significant offsets in the KK-residuals at an applied DC bias offset of 1.0 V may be due to the limited linear response of the PSC in the current–voltage characteristics at such high applied voltages. Additionally, the formation of PbI<sub>2</sub> has been reported in MAPbI<sub>2</sub> at high applied biases.<sup>69</sup>

The analysis of the KK-residuals appears to offer detailed insight into frequency-dependence of electrochemical loss processes, as these generally result in a non-linear IS response. In the case of multiple electrochemical processes, such as ion migration, chemical reactions, electrode polarization, with overlapping frequency responses, the KK residuals may offer insight to guide ECM analysis.



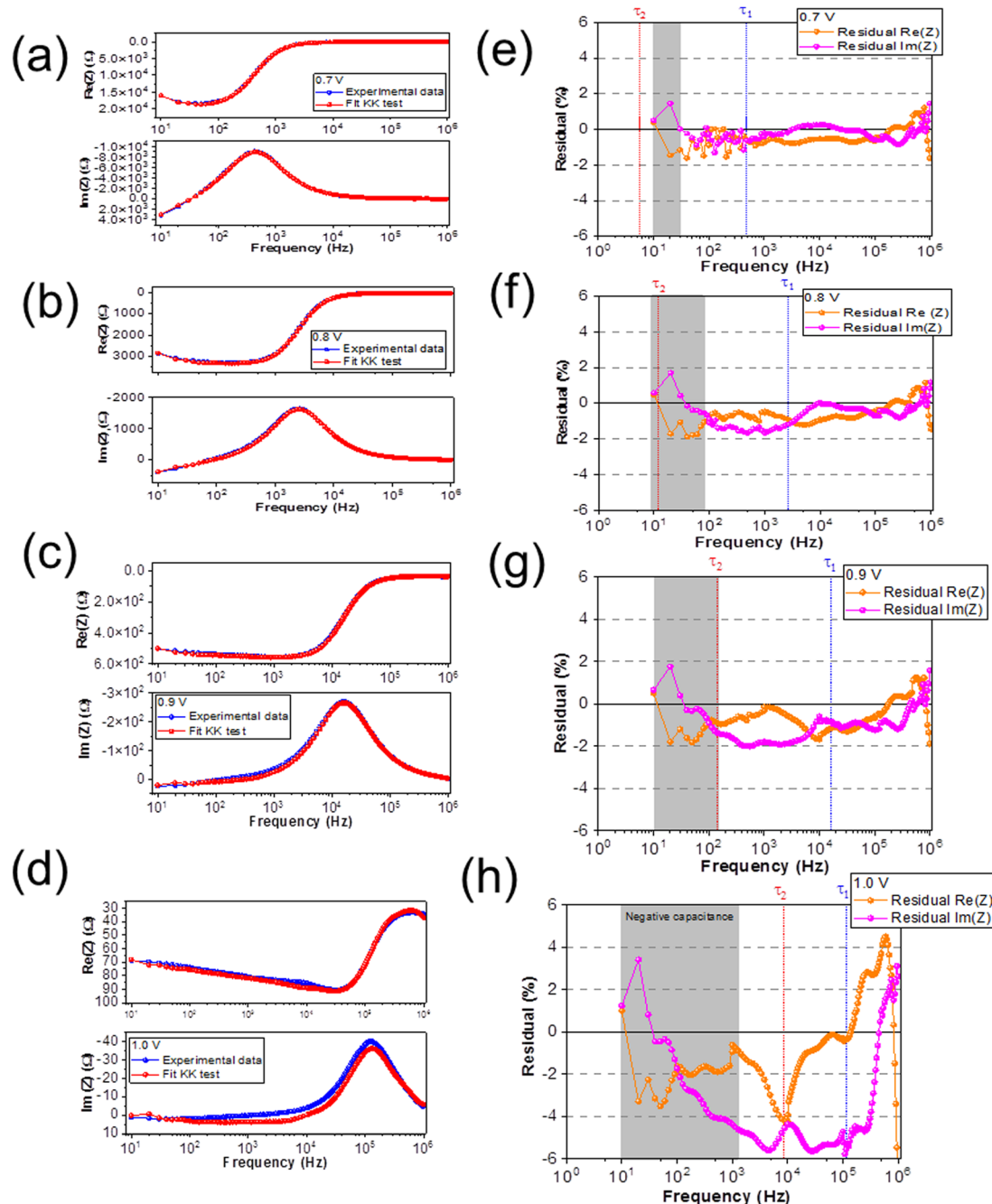


**Fig. 6** (a–d) The experimental data (blue) as well as the KK fit (red) of  $\text{Re}(Z)$  and  $\text{Im}(Z)$  versus frequency at DC bias of 0.7 V, 0.8 V, 0.9 V, and 1.0 V, respectively; (e–h) the residuals from the KK fit versus frequency at DC bias of 0.7 V, 0.8 V, 0.9 V and 1.0 V, respectively. The orange data represents the residual from  $\text{Re}(Z)$  and the pink data represents the residual from  $\text{Im}(Z)$ , respectively. The frequencies that correspond to the relaxation times with a vertically dashed line in each spectrum (the HF (blue) and LF (red) peak), while highlighted the data points (gray) that correspond to the negative capacitive tail.

We identify and quantify electrochemical dynamics in  $\text{MAPbI}_3$  PSC using IS studies combined with a universal ECM. The HF and LF dynamics are ubiquitously separated by several orders of magnitude in the frequency spectrum in PSC, enabling a robust fitting procedure to distinguish electrical and electrochemical processes. We show how the HF response can be analyzed to extract accurate values for the PSC permittivity. Analysis of the LF dynamics reveals detailed insight into

loss processes in the PSC, specifically ionic dynamics which we attribute to  $\text{MA}^+$  and  $\text{I}^-$  migration in the  $\text{MAPbI}_3$  absorber layers. The KK-residuals, which are generally used as an indication of the quality of IS data, can be used to shed light on the timescale and the nature of the electrochemical dynamics. We show how the voltage and frequency dependence of the residuals can offer more detailed information than the Nyquist plot on specific slow and/or irreversible dynamics related to losses



in the PSC. Our approach represents a fast and straightforward method for screening and evaluating materials and fabrication procedures on PSC stability and lifetime.

### 3. Experimental section

#### 3.1. Solar cells fabrication

**3.1.1. Deposition of TiO<sub>2</sub> as ETL.** TiO<sub>2</sub> was deposited on top of ITO glass substrate. The substrates were covered by foil, then they were firstly cleaned by acetone. Next, the substrate were immersed in 25 mL of soap (Extran MA02) in 175 mL of demi water, then sonicate for 5 minutes. Afterwards, the substrates was rinsed with demi water, and sonicate again for 5 minutes. Subsequently, the substrate were sonicated in iso-propanol for 5 minutes and was dried using N<sub>2</sub> gases spray. Then, 2 hours before TiO<sub>2</sub> deposition, the substrates was cleaned by the UV/Ozone cleaner for 30 minutes. Finally, TiO<sub>2</sub> were deposited by e-beam deposition with rate 0.1 nm s<sup>-1</sup>. Resulting of the thickness of 50 nm.

**3.1.2. Depositing of MAPbI<sub>3</sub> as absorber layer.** The MAPbI<sub>3</sub> was deposited using spincoating by one-step deposition from the mixtures of solution of MAI: lead acetate (PbAc<sub>2</sub>) and the solution of the MAI: lead chloride (PbCl<sub>2</sub>), in Dimethylformamide (DMF) with the addition of H<sub>2</sub>O. Here, weigh 222 mg of PbCl<sub>2</sub> and 382 mg of MAI was dissolved in 1 mL DMF in the glovebox under N<sub>2</sub> ambient. The solution was stirred for at least 10 minutes at room temperature. While, weigh 259 mg of PbAc<sub>2</sub> and 382 mg of MAI was dissolved in 0.76 mL DMF and then was stirred the solution at least 10 minutes at room temperature in the glovebox under N<sub>2</sub> ambient. The PbAc<sub>2</sub> was dried in the vacuum oven overnight before used. Then, the mixture of MAI: PbCl<sub>2</sub> and MAI:PbAc<sub>2</sub> solution was made from 0.24 mL of the MAI:PbCl<sub>2</sub> solution into 0.76 mL of MAI:PbAc<sub>2</sub> and then was stirred again at least 5 minutes at room temperature. 50 μL of H<sub>2</sub>O was added into the solution of MAI:PbCl<sub>2</sub> and MAI:PbAc<sub>2</sub> mixture outside the glovebox and stir again at least 10 minutes at room temperature in the glovebox under N<sub>2</sub> ambient. Afterward the solution of the MAI:PbCl<sub>2</sub> and MAI: PbAc<sub>2</sub> was deposited on top of TiO<sub>2</sub> by spincoating at 3000 rpm, ramp 5000 rpm s<sup>-1</sup> for duration 60 s. Then the sample was thermally annealed at the temperature ramps from 90 °C to 130 °C in 5 minutes, then keep 10 minutes at temperature of 130 °C.

In general the formation of the MAPbI<sub>3</sub> can be described by the following reaction:<sup>34</sup>



where CH<sub>3</sub>NH<sub>3</sub>I is MAI, while X can be Cl, I and acetate group (Ac). This reaction typically involved the evaporation solvent as product (CH<sub>3</sub>NH<sub>3</sub>X).<sup>34</sup>

**3.1.3. Deposition of doped Spiro-OMeTAD as the HTL.** 80 mg of Spiro-OMeTAD was dissolved in 1 mL of Chlorobenzene. The solution was then stirred overnight in the glovebox. 28.5 μL 4-*tert*-butyl pyridine, followed by 17.5 μL of Lithium bistrifluoromethanesulphonimide solution (520 mg Lithium bistrifluoro – methanesulphonimide/1 mL acetonitrile) were

then added to the solution. The final solution was then stirred for 10 min. 50 μL of the solution was deposited on top of the perovskite layer by spincoating at 2000 rpm for 60 s. The sample was purged in N<sub>2</sub> for 30 minutes. The samples were then exposed for at least one night to ambient conditions in the dark.

**3.1.4. Deposition Au electrode.** Finally, to complete fabrication of the solar cells device, 100 nm of Au was deposited using a thermal evaporator with a deposition rate of 0.1 nm s<sup>-1</sup> at 1 × 10<sup>-6</sup> mbar.

#### 3.2. *J-V* characterization

The *J-V* measurements were performed in the dark and under standard AM 1.5 illumination (100 mW cm<sup>-2</sup>) with a solar simulator in an N<sub>2</sub> environment. The *J-V* scan were conducted start from 1.2 V to -1 V. Light soaking was applied for 2 minutes before *J-V* scan under illumination. The sample mask which of 0.038 cm<sup>2</sup>, 0.089 cm<sup>2</sup>, 0.249 cm<sup>2</sup>, and 0.805 cm<sup>2</sup> active areas were used on the *J-V* measurement under illumination, respectively. The active areas of the every samples without masked consisting of 0.09 cm<sup>2</sup>, 0.16 cm<sup>2</sup>, 0.36 cm<sup>2</sup>, and 1.0 cm<sup>2</sup>, respectively.

#### 3.3. Impedance spectroscopy

IS measurements were performed using an GSTAT302N (Autolab, Metrohm) with an impedance analyzer (FRA3M). We performed the IS measurement on the solar cells device in the dark at DC bias of 0.7 V, 0.8 V, 0.9 V and 1.0 V. The impedance measurement was conducted from 1 MHz to 10 Hz using the AC voltage amplitude of 20 mV.

#### 3.4. PL spectroscopy

PL measurements of perovskite were conducted at 470 nm of excitation wave length, with parameters of excitation filters from 335–620 nm and the emission filters from 550–1100 nm, respectively.

### Author contributions

All authors have given approval to the final version of the manuscript.

### Conflicts of interest

The authors declare no competing financial interest.

### Acknowledgements

Tulus acknowledges the National Research and Innovation Agency (BRIN), the Republic of Indonesia for the scholarship Program for Research and Innovation in Science and Technology (RISET-Pro) World Bank Loan No. 8245-ID. Tulus, Elizabeth von Hauff and Yulia Galagan acknowledge the COST Action Stable Next Generation Photovoltaics (Grant No. MP1307) for support.



## References

- 1 J. Y. Kim, J. W. Lee, H. S. Jung, H. Shin and N. G. Park, *Chem. Rev.*, 2020, **120**, 7867–7918.
- 2 M. Saliba, O. M. Bakr, N. Pradhan, M. Kuno and P. V. Kamat, *ACS Energy Lett.*, 2019, **4**, 3036–3038.
- 3 Y. Zhou and M. Saliba, *ACS Energy Lett.*, 2021, **6**, 2750–2754.
- 4 K. M. Yeom, S. U. Kim, M. Y. Woo, J. H. Noh and S. H. Im, *Adv. Mater.*, 2020, **32**, 2002228.
- 5 J. Liang and Y. B. Qi, *Mater. Today Nano*, 2021, **16**, 100143.
- 6 J. Jeong, M. Kim, J. Seo, H. Lu, P. Ahlawat, A. Mishra, Y. Yang, M. A. Hope, F. T. Eickemeyer, M. Kim, Y. J. Yoon, I. W. Choi, B. P. Darwich, S. J. Choi, Y. Jo, J. H. Lee, B. Walker, S. M. Zakeeruddin, L. Emsley, U. Rothlisberger, A. Hagfeldt, D. S. Kim, M. Grätzel and J. Y. Kim, *Nature*, 2021, **592**, 381–385.
- 7 J. Chen, D. He and N. G. Park, *Sol. RRL*, 2022, **6**, 2100767.
- 8 N. G. Park, *Adv. Energy Mater.*, 2019, **1903106**, 1–14.
- 9 S. I. Seok, M. Grätzel and N. G. Park, *Small*, 2018, **14**(20), 1–17.
- 10 H. J. Snaith, *J. Phys. Chem. Lett.*, 2013, **4**, 3623–3630.
- 11 M. Kim, J. Jeong, H. Lu, T. K. Lee, F. T. Eickemeyer, Y. Liu, I. W. Choi, S. J. Choi, Y. Jo, H. B. Kim, S. I. Mo, Y. K. Kim, H. Lee, N. G. An, S. Cho, W. R. Tress, S. M. Zakeeruddin, A. Hagfeldt, J. Y. Kim, M. Grätzel and D. S. Kim, *Science*, 2022, **375**, 302–306.
- 12 E. J. Juarez-Perez and M. Haro, *Science*, 2020, **368**(6497), 1309.
- 13 H. Lu, A. Krishna, S. M. Zakeeruddin, M. Grätzel and A. Hagfeldt, *iScience*, 2020, **23**(101359), 1–14.
- 14 Y. Chen, S. Tan, N. Li, B. Huang, X. Niu, L. Li, M. Sun, Y. Zhang, X. Zhang, C. Zhu, N. Yang, H. Zai, Y. Wu, S. Ma, Y. Bai, Q. Chen, F. Xiao, K. Sun and H. Zhou, *Joule*, 2020, **4**(9), 1961–1976.
- 15 J. J. Yoo, G. Seo, M. R. Chua, T. G. Park, Y. Lu, F. Rotermund, Y. K. Kim, C. S. Moon, N. J. Jeon, J. P. Correa-Baena, V. Bulović, S. S. Shin, M. G. Bawendi and J. Seo, *Nature*, 2021, **590**(2), 587–593.
- 16 D. Luo, R. Su, W. Zhang, Q. Gong and R. Zhu, *Nat. Rev. Mater.*, 2019, **5**, 44–60.
- 17 J. F. Guillemoles, T. Kirchartz, D. Cahen and U. Rau, *Nat. Photonics*, 2019, **13**(8), 501–505.
- 18 A. Sharenko and M. F. Toney, *J. Am. Chem. Soc.*, 2016, **138**, 463–470.
- 19 L. K. Ono, S. F. Liu and Y. Qi, *Angew. Chem., Int. Ed.*, 2020, **59**, 6676–6698.
- 20 E. M. Hutter, J. J. Hofman, M. L. Petrus, M. Moes, R. D. Abellon, P. Docampo and T. J. Savenije, *Adv. Energy Mater.*, 2017, **7**, 1602349.
- 21 Tulus, S. Olthof, M. Marszalek, A. Peukert, L. A. Muscarella, B. Ehrler, O. Vukovic, Y. Galagan, S. C. Boehme and E. Von Hauff, *ACS Appl. Energy Mater.*, 2019, **2**(5), 3736–3748.
- 22 P. Schulz, D. Cahen and A. Kahn, *Chem. Rev.*, 2019, **119**(5), 3349–3417.
- 23 A. Kojima, K. Teshima, Y. Shirai and T. Miyasaka, *J. Am. Chem. Soc.*, 2009, **131**, 6050–6051.
- 24 M. M. Lee, J. Teuscher, T. Miyasaka, T. N. Murakami and H. J. Snaith, *Science*, 2012, **338**, 643–647.
- 25 Y. Wu, F. Xie, H. Chen, X. Yang, H. Su, M. Cai, Z. Zhou, T. Noda and L. Han, *Adv. Mater.*, 2017, **29**, 1701073.
- 26 L. McGovern, M. H. Futscher, L. A. Muscarella and B. Ehrler, *J. Phys. Chem. Lett.*, 2020, **11**, 7127–7132.
- 27 T. B. Song, Q. Chen, H. Zhou, C. Jiang, H. H. Wang, Y. M. Yang, Y. Liu, J. You and Y. Yang, *J. Mater. Chem. A*, 2015, **3**, 9032–9050.
- 28 Q. Lin, A. Armin, R. Chandra, R. Nagiri, P. L. Burn and P. Meredith, *Nat. Photonics*, 2015, **9**, 106–112.
- 29 M. A. Green and S. P. Bremner, *Nat. Mater.*, 2017, **16**(1), 23–34.
- 30 J. W. Lee, D. H. Kim, H. S. Kim, S. W. Seo, S. M. Cho and N. G. Park, *Adv. Energy Mater.*, 2015, **5**, 1501310.
- 31 S. H. Turren-Cruz, A. Hagfeldt and M. Saliba, *Science*, 2018, **362**, 449–453.
- 32 J. Wei, Q. Wang, J. Huo, F. Gao, Z. Gan, Q. Zhao and H. Li, *Adv. Energy Mater.*, 2021, **11**, 2002326.
- 33 J. B. Patel, R. L. Milot, A. D. Wright, L. M. Herz and M. B. Johnston, *J. Phys. Chem. Lett.*, 2016, **7**, 96–102.
- 34 W. Zhang, M. Saliba, D. T. Moore, S. K. Pathak, M. T. Horantner, T. Stergiopoulos, S. D. Stranks, G. E. Eperon, J. A. Alexander-Webber, A. Abate, A. Sadhanala, S. Yao, Y. Chen, R. H. Friend, L. A. Estroff, U. Wiesner and H. J. Snaith, *Nat. Commun.*, 2015, **6**(6142), 1–10.
- 35 B. Conings, A. Babayigit, T. Vangerven, J. D'Haen, J. Manca and H. G. Boyen, *J. Mater. Chem. A*, 2015, **3**, 19123–19128.
- 36 L. Ling, S. Yuan, P. Wang, H. Zhang, L. Tu, J. Wang, Y. Zhan and L. Zheng, *Adv. Funct. Mater.*, 2016, **26**, 5028–5034.
- 37 M. Alsari, O. Bikondo, J. Bishop, M. Abdi-Jalebi, L. Y. Ozer, M. Hampton, P. Thompson, M. T. Horantner, S. Mahesh, C. Greenland, J. E. Macdonald, G. Palmisano, H. J. Snaith, D. G. Lidzey, S. D. Stranks, R. H. Friend and S. Lilliu, *Energy Environ. Sci.*, 2018, **11**, 383–393.
- 38 D. P. McMeekin, G. Sadoughi, W. Rehman, G. E. Eperon, M. Saliba, M. T. Hörlantner, A. Haghighirad, N. Sakai, L. Korte, B. Rech, M. B. Johnston, L. M. Herz and H. J. Snaith, *Science*, 2016, **351**(6269), 151–155.
- 39 M. Saliba, T. Matsui, K. Domanski, J. Y. Seo, A. Ummadisingu, S. M. Zakeeruddin, J.-P. Correa-Baena, W. R. Tress, A. Abate, A. Hagfeldt and M. Grätzel, *Science*, 2016, **354**(6309), 206–209.
- 40 M. Saliba, T. Matsui, J. Y. Seo, K. Domanski, J. P. Correa-Baena, M. K. Nazeeruddin, S. M. Zakeeruddin, W. Tress, A. Abate, A. Hagfeldt and M. Grätzel, *Energy Environ. Sci.*, 2016, **9**(6), 1989–1997.
- 41 S. Mahesh, J. M. Ball, R. D. J. Oliver, D. P. McMeekin, B. Johnston and H. J. Snaith, *Energy Environ. Sci.*, 2020, **13**, 258–267.
- 42 H. Li and W. Zhang, *Chem. Rev.*, 2020, **120**, 9835–9950.
- 43 H. J. Snaith, *Nat. Mater.*, 2018, **17**, 372–376.
- 44 E. L. Unger, A. R. Bowering, C. J. Tassone, V. Pool, A. Gold-Parker, R. Cheacharoen, K. H. Stone, E. T. Hoke, M. F. Toney and M. D. McGehee, *Chem. Mater.*, 2014, **26**(24), 7158–7165.
- 45 E. von Hauff and D. Klotz, *J. Mater. Chem. C*, 2022, **10**(2), 742–761.
- 46 G. Y. Kim, A. Senocrate, T. Y. Yang, G. Gregori, M. Grätzel and J. Maier, *Nat. Mater.*, 2018, **17**, 445–449.
- 47 F. Ebadi, N. Taghavinia, R. Mohammadpour, A. Hagfeldt and W. Tress, *Nat. Commun.*, 2019, **10**(1574), 1–9.



- 48 J. Lim, M. T. Horantner, N. Sakai, J. M. Ball, S. Mahesh, N. K. Noel, Y. H. Lin, J. B. Patel, D. P. McMeekin, M. B. Johnston, B. Wenger and H. J. Snaith, *Energy Environ. Sci.*, 2019, **12**(1), 169–176.
- 49 B. Hailegnaw, N. S. Sariciftci and M. C. Scharber, *Phys. Status Solidi A*, 2020, **217**, 2000291.
- 50 D. Klotz, *Electrochem. Commun.*, 2019, **98**(11), 58–62.
- 51 A. J. Riquelme, K. Valadez-Villalobos, P. P. Boix, G. Oskam, I. Mora-Seró and J. A. Anta, *Phys. Chem. Chem. Phys.*, 2022, **24**(26), 15657–15671.
- 52 R. S. Sanchez, V. Gonzalez-Pedro, J. W. Lee, N. G. Park, Y. S. Kang, I. Mora-Sero and J. Bisquert, *Phys. Chem. Lett.*, 2014, **5**(13), 2357–2363.
- 53 J. Seo, J. H. Noh and S. I. Seok, *Acc. Chem. Res.*, 2016, **49**(3), 562–572.
- 54 M. Grätzel, *Nat. Mater.*, 2014, **13**(9), 838–842.
- 55 W. Nie, J. C. Blancon, A. J. Neukirch, K. Appavoo, H. Tsai, M. Chhowalla, M. A. Alam, M. Y. Sfeir, C. Katan, J. Even, S. Tretiak, J. J. Crochet, G. Gupta and A. D. Mohite, *Nat. Commun.*, 2016, **7**(11574), 1–9.
- 56 Tulus, L. A. Muscarella, Y. Galagan, S. C. Boehme and E. von Hauff, *Electrochim. Acta*, 2022, **433**, 141215.
- 57 H. S. Kim, C. R. Lee, J. H. Im, K. B. Lee, T. Moeh, A. Marchioro, S. J. Moon, R. H. Baker, J. H. Yum, J. E. Moser, M. Gratzel and N. G. Park, *Sci. Rep.*, 2012, **2**(591), 1–7.
- 58 W. J. Scheideler, N. Rolston, O. Zhao, J. Zhang and R. H. Dauskardt, *Adv. Energy Mater.*, 2019, 1803600.
- 59 T. Leijtens, G. E. Eperon, S. Pathak, A. Abate, M. M. Lee and H. J. Snaith, *Nat. Commun.*, 2013, **4**(2885), 1–8.
- 60 B. Ecker, H. Egelhaaf, R. Steim, J. Parisi and E. von Hauff, *J. Phys. Chem. C*, 2012, **116**, 16333–16337.
- 61 Y. Lu, Z. Si, H. Liu, Y. Ge, J. Hu, Z. Zhang, X. Mu, K. Selvakumar and M. Sui, *Chem. – Eur. J.*, 2021, **27**, 3729–3736.
- 62 A. Alberti, I. Deretzis, G. Pellegrino, C. Bongiorno, E. Smecca, G. Mannino, F. Giannazzo, G. G. Condorelli, N. Sakai, T. Miyasaka, C. Spinella and A. La Magna, *Chem. Phys. Chem.*, 2015, **16**, 3064–3071.
- 63 E. von Hauff, *J. Phys. Chem. C*, 2019, **123**, 11329–11346.
- 64 D. Klotz, G. Tumen-ulzii, C. Qin, T. Matsushima and C. Adachi, *RSC Adv.*, 2019, **9**, 33436–33445.
- 65 A. O. Alvarez, R. Arcas, C. A. Aranda, L. Bethencourt, E. Mas-Marzá, M. Saliba and F. Fabregat-Santiago, *J. Phys. Chem. Lett.*, 2020, **11**, 8417–8423.
- 66 Z. S. Wang, F. Ebadi, B. Carlsen, W. C. H. Choy and W. Tress, *Small Methods*, 2020, **4**, 2000290.
- 67 J. N. Wilson, J. M. Frost, S. K. Wallace and A. Walsh, *APL Mater.*, 2019, **7**, 010901.
- 68 M. H. Futscher, J. M. Lee, L. McGovern, L. A. Muscarella, T. Wang, M. I. Haider, A. Fakhruddin, L. Schmidt-Mende and B. Ehrler, *Mater. Horiz.*, 2019, **6**, 1497–1503.
- 69 Y. Yuan, Q. Wang, Y. Shao, H. Lu, T. Li, A. Gruverman and J. Huang, *Adv. Energy Mater.*, 2016, **6**, 1501803.
- 70 S. Thampy, B. Zhang, K. H. Hong, K. Cho and J. W. P. Hsu, *ACS Energy Lett.*, 2020, **5**(4), 1147–1152.
- 71 A. M. A. Leguy, Y. Hu, M. Campoy-Quiles, M. I. Alonso, O. J. Weber, P. Azarhoosh, M. van Schilfgaarde, M. T. Weller, T. Bein, J. Nelson, P. Docampo and Piers R. F. Barnes, *Chem. Mater.*, 2015, **27**, 3397–3407.
- 72 M. Schönleber and E. Ivers-Tiffée, *Electrochem. Commun.*, 2015, **58**, 15–19.
- 73 M. Schönleber, D. Klotz and E. Ivers-Tiffée, *Electrochim. Acta*, 2014, **131**, 20–27.
- 74 B. A. Boukamp, *J. Electrochem. Soc.*, 1995, **142**(6), 1885–1894.
- 75 S. Reichert, Q. An, Y. W. Woo, A. Walsh, Y. Vaynzof and C. Deibe, *Nat. Commun.*, 2020, **11**, 6098.

